


Cite this: *RSC Adv.*, 2024, 14, 1216

# A theoretical investigation on the structural stability, superconductivity, and optical and thermodynamic properties of Ir<sub>2</sub>P under pressure†

Xiao-Wei Sun,<sup>\*ab</sup> Meng-Ru Chen,<sup>id a</sup> Xi-Long Dou,<sup>b</sup> Ning Li,<sup>b</sup> Tong Wang<sup>b</sup> and Ting Song<sup>b</sup>

The potential applications of Ir<sub>2</sub>P are promising due to its desirable hardness, but its fundamental properties are still not fully understood. In this study, we present a systematic investigation of Ir<sub>2</sub>P's structural, electronic, superconducting, optical, and thermodynamic properties of Ir<sub>2</sub>P under pressure. Our calculations show that Ir<sub>2</sub>P has a *Fm* $\bar{3}$ *m* structure at ambient pressure, which matches well with experimental data obtained from high-pressure synchrotron X-ray diffraction. As pressure increases, a transition from the *Fm* $\bar{3}$ *m* to the *I4*/*mmm* phase occurs at 103.4 GPa. The electronic structure and electron-phonon coupling reveal that the *Fm* $\bar{3}$ *m* and *I4*/*mmm* phases of Ir<sub>2</sub>P are superconducting materials with superconducting transition temperatures of 2.51 and 0.89 K at 0 and 200 GPa, respectively. The optical properties of Ir<sub>2</sub>P indicate that it has optical conductivity in the infrared, visible, and ultraviolet regions. Additionally, we observed that the reflectivity *R*( $\omega$ ) of Ir<sub>2</sub>P is higher than 76% in the 25–35 eV energy range at different pressures, which suggests that it could be used as a reflective coating. We also explored the finite-temperature thermodynamic properties of Ir<sub>2</sub>P, including the Debye temperature, the first and second pressure derivatives of the isothermal bulk modulus, and the thermal expansion coefficient up to 2000 K using the quasi-harmonic Debye model. Our findings offer valuable insights for engineers to design better devices.

Received 2nd November 2023  
Accepted 20th December 2023

DOI: 10.1039/d3ra07464a

rsc.li/rsc-advances

## 1. Introduction

The combination of 4d and 5d transition metals with low-*Z* elements (IIIA–VIA) has been proven to be an effective strategy for designing new hard and superhard materials.<sup>1–3</sup> The idea is that the high electron concentration of transition metals and the directional bonding created by strong hybridizations between d electrons of transition metals and s, p electrons of light (low-*Z*) elements can effectively withstand both elastic and plastic deformations.<sup>4</sup> Some promising candidates, such as OsB<sub>2</sub>, Ir<sub>4</sub>B<sub>5</sub>, ReB<sub>2</sub>, WB<sub>4</sub>, TaC, ReC, ReC<sub>2</sub>, Zr<sub>3</sub>N<sub>4</sub>, and Mo<sub>3</sub>N<sub>5</sub> have been experimentally synthesized and studied.<sup>5–13</sup> First-principles density functional theory (DFT) calculations are a powerful tool for predicting the structural, electronic, elastic, and thermodynamic properties of carbides, nitrides and borides with transition-metal elements in a large region of the periodic table.<sup>14–23</sup> However, the study of transition-metal

phosphides (TMPs), especially noble-metal phosphides, is relatively limited.

TMPs are a group of compounds that possess unique chemical and physical properties. These properties make them highly attractive for potential applications in various fields, such as photonics, electronics, magnetism, hard materials, and catalysis.<sup>24–26</sup> Systematic computational investigations have shown that phosphorus atoms in TMPs play a crucial role in hydrogen evolution reactions.<sup>27</sup> Phosphorus atoms with higher electronegativity can draw electrons from metal atoms, and negatively charged phosphate groups can act as a base in electrochemical hydrogen evolution reactions. Generally, TMPs with a higher metal content exhibit more metallic characteristics because metal atoms contribute more electrons to the compound, leading to a lower overall electronegativity and a more metallic nature. Additionally, as the atomic ratio of phosphorus to metal increases, the bonding between the phosphorus and metal atoms becomes weaker, which can also promote metallic behavior.<sup>28</sup> Silica-supported palladium and ruthenium phosphide catalysts, such as Pd<sub>3</sub>P, Pd<sub>5</sub>P<sub>2</sub>, Ru<sub>2</sub>P, and RuP, were recently synthesized and studied by Bowker *et al.*<sup>29</sup> to investigate the hydrodesulfurization properties of dibenzothiophene. The properties of these phases were compared with those of the sulfides of the noble metals. Although Ir<sub>2</sub>P was first reported in 1935 by Blatz *et al.*,<sup>30</sup> there have been comparatively

<sup>a</sup>School of Mechanical Engineering, Lanzhou Jiaotong University, Lanzhou 730070, PR China. E-mail: sunxw\_lzjtu@yeah.net

<sup>b</sup>School of Mathematics and Physics, Lanzhou Jiaotong University, Lanzhou 730070, PR China

† Electronic supplementary information (ESI) available. See DOI: <https://doi.org/10.1039/d3ra07464a>


few studies of its synthesis routes and crystal structures. Rundqvist *et al.*<sup>31</sup> examined the crystal structures of three phosphides, namely, Rh<sub>2</sub>P and Ir<sub>2</sub>P with the anti-fluorite structure and PtP<sub>2</sub> with the pyrite structure. Raub *et al.*<sup>32</sup> discovered that only the Ir<sub>2</sub>P exhibited a metallic behavior among the family of Ir<sub>2</sub>X and IrX (where X = P, As, Sb, and Bi) Pt-metal alloys. Sweeney *et al.*<sup>33</sup> explored the feasibility of hydrogen reduction annealing of metal phosphates as a selected pathway to phosphides for rhodium and iridium. Unfortunately, there is limited information available on the high-pressure properties of Ir<sub>2</sub>P due to the difficulty in synthesizing it, even though high-pressure synthesis is a powerful method for preparing novel materials with unique electrical and mechanical properties. In 2016, Ir<sub>2</sub>P was successfully synthesized under high-pressure conditions, and it was found to have an anti-fluorite structure with space group *Fm* $\bar{3}$ *m*, as determined from synchrotron X-ray diffraction (XRD) pattern analysis. The structure remains stable at room temperature and pressures ranging from 0 to 40.6 GPa. In this structure, each Ir atom is surrounded by four P atoms, forming [IrP<sub>4</sub>] tetrahedrons, which are located at the edges of the unit cell.<sup>34</sup> Research indicates that Ir<sub>2</sub>P has a significant bulk modulus (*B*) (320 and 342 GPa) and a relatively modest shear modulus (*G*) (42 and 64 GPa) derived from generalized gradient approximation (GGA) and local density approximation (LDA) calculations respectively. This indicates a complex bonding profile for Ir<sub>2</sub>P, encompassing metallic, ionic, and covalent characteristics. Subsequently, the ground-state structure of Ir<sub>2</sub>P is predicted to be *Fm* $\bar{3}$ *m*, while the high-pressure structure is expected to be *I4*/*mmm*. It was shown that the predicted ground-state structure is consistent with the experimentally obtained structure and its phase transition pressure is 86.4 GPa.<sup>35</sup>

We have conducted a comprehensive theoretical analysis of Ir<sub>2</sub>P, a material about which limited information is available. Our analysis is based on first-principles calculations within the framework of DFT using GGA and LDA. We have optimized its geometric structure and explored its energy-volume equation of state (EOS), as well as delving into its electronic band structures, elastic properties, and superconductivity characteristics. We have also predicted the complex dielectric function, reflectivity, absorption coefficient, optical conductivity, and loss function of Ir<sub>2</sub>P to obtain the regular behavior of these optical parameters with pressure. Additionally, we have predicted the finite-temperature thermodynamic properties of cubic Ir<sub>2</sub>P, including the isothermal bulk modulus, and its first and second pressure derivatives, thermal expansion coefficient, and Debye temperature at the atomic level by means of density functional total energy calculations in combination with the quasi-harmonic Debye (QHD) model. These findings can potentially guide further research and help in the development of practical applications for this material.

## 2. Theoretical methods

The Vienna *ab initio* Simulation Package (VASP) code, within the framework of DFT, was used to calculate the mechanical and electronic properties of Ir<sub>2</sub>P.<sup>36</sup> The interaction between valence electrons and ions in Ir<sub>2</sub>P was modeled using the

ultrasoft pseudopotential.<sup>37</sup> The exchange and correlation potentials were described by the GGA-PBESol<sup>38</sup> and the LDA,<sup>39</sup> respectively. The use of ultrasoft pseudopotentials can provide a more accurate description of the electronic structure of materials, especially for systems with complex valence-electron configurations like Ir and P, where 5d<sup>7</sup> 6s<sup>2</sup> and 3s<sup>2</sup> 3p<sup>3</sup> selected should be compatible with the special type of GGA or LDA. After the convergence test, the Brillouin zone integrations for the primitive unit cell of *Fm* $\bar{3}$ *m* and *I4*/*mmm* structures were sampled using 12 × 12 × 12 and 15 × 15 × 18 meshes according to the Monkhorst–Pack method with plane-wave cut-off energies of 600 and 850 eV, respectively.<sup>40</sup> The BFGS minimization technique was used in the geometry optimization at different hydrostatic pressures ranging from 0 to 200 GPa, after which elastic constants were calculated.<sup>41</sup> Prior research has suggested that the BFGS minimization technique is capable of providing a fast way of finding the lowest energy structure.

In this study, a convergence threshold was set at 5.0 × 10<sup>−7</sup> eV per atom, to determine if the iterative process of updating the electronic wave functions and potentials has reached a stable solution, for the self-consistent progress. The convergence criterion for energy, force, ionic displacement, and stress were set to 5.0 × 10<sup>−6</sup> eV per atom, 0.01 eV Å<sup>−1</sup>, 5.0 × 10<sup>−4</sup> Å, and 0.02 GPa, respectively. When calculating elastic properties, the force on the atom refers to the force applied to the atom during the simulation, while the atomic position displacement refers to the change in the position of the atoms between computational cycles. To prevent excessive strain on the atom and maintain the stability of the simulation, these values are limited to 0.002 eV Å<sup>−1</sup> and 1.0 × 10<sup>−4</sup> Å, respectively. The maximum strain amplitude is set to be 0.003, which is the maximum amount the atoms can be deformed during the simulation. Six distorted structures were generated within this limit, likely for further analysis or study. These parameters and settings were chosen to ensure that the calculated elastic properties are accurate and reliable, while also maintaining computational efficiency.

The strained energy for cubic and tetragonal Ir<sub>2</sub>P is expressed by the law from ref. 42. The mechanical stability criteria obtained from elastic stiffness coefficients can be found in ref. 43 or 44. Currently, the stress–strain method is being used. The phonon dispersions for *Fm* $\bar{3}$ *m* and *I4*/*mmm* structures were calculated on 2 × 2 × 2 supercells which contain 48 and 96 atoms, respectively, using density-functional perturbation theory (DFPT) method implemented in the PHONOPY code.<sup>45</sup> The forces result from VASP.

The electron-phonon coupling (EPC) calculations for Ir<sub>2</sub>P were performed using the QUANTUM-ESPRESSO package<sup>46</sup> with ultrasoft pseudopotential for core-valence interaction. The kinetic energy cutoff of 60 Ry was chosen as the plane-wave expansion. The *k* meshes and *q* meshes of 12 × 12 × 12 and 3 × 3 × 3, 24 × 24 × 12 and 3 × 3 × 2 were selected as the first Brillouin zone for *Fm* $\bar{3}$ *m* and *I4*/*mmm* of Ir<sub>2</sub>P, respectively. Taking into account that the EPC parameters  $\lambda$  of *I4*/*mmm* for Ir<sub>2</sub>P is smaller than 1.5, the superconducting transition temperature (*T*<sub>c</sub>) is estimated through McMillan equation<sup>47</sup>

$$T_c = \frac{\omega_{\log}}{1.2} \exp \left[ -\frac{1.04(1+\lambda)}{\lambda - \mu^*(1+0.62\lambda)} \right], \quad (1)$$

where  $\mu^*$  is the effective Coulomb pseudopotential, and  $\omega_{\log}$  is the logarithmic average frequency, which is expressed as

$$\omega_{\log} = \exp \left[ \frac{2}{\lambda} \int_0^{\infty} \frac{\alpha^2 F(\omega) \log(\omega)}{\omega} d\omega \right], \quad (2)$$

where  $\lambda$  is the EPC parameter, defined as

$$\lambda = 2 \int_0^{\infty} \frac{\alpha^2 F(\omega)}{\omega} d\omega, \quad (3)$$

The complex dielectric function  $\varepsilon(\omega)$  is often used to characterize the optical properties of a material. Due to the metallic nature of  $\text{Ir}_2\text{P}$ , a semi-exponential Drude term and Gaussian smearing of 0.5 eV are used to calculate the frequency-dependent dielectric constants<sup>48</sup>

$$\varepsilon(\omega) = \varepsilon_1(\omega) + i\varepsilon_2(\omega). \quad (4)$$

In the formula above, the complex dielectric function,  $\varepsilon(\omega)$ , is a complex number representing the ratio of the electric field to the electric displacement in a material. The symbol  $\omega$  refers to the frequency of the incident photon, while  $\varepsilon_1(\omega)$  and  $\varepsilon_2(\omega)$  refers to the real and imaginary parts of the complex dielectric function, respectively. The  $\varepsilon_2(\omega)$  value is calculated from the momentum matrix element between the occupied and unoccupied electronic states, and the  $\varepsilon_1(\omega)$  is derived from the imaginary part using the Kramers–Kronig relation.

To study the behavior of  $\text{Ir}_2\text{P}$  under finite temperature conditions, a QHD model was used to determine the Debye temperature, isothermal bulk modulus, and its first and second pressure derivatives, as well as the thermal expansion coefficient. These properties are important thermodynamic characteristics of materials. The GIBBS software program<sup>49</sup> was used to implement the QHD model.

Since Ir is a metal containing d electrons, we explore the magnetism of the  $Fm\bar{3}m$  and  $I4/mmm$  phases. We perform energy mapping of all conceivable magnetic configurations and calculate the spin-polarized density of states for both phases, as shown in Fig. S1 and S2.† The absence of a non-zero magnetic moment per Ir atom in the considered magnetic configurations, and the symmetric density of states, confirmed that both phases are nonmagnetic. Therefore, this study does not incorporate spin polarization.

## 3. Results and discussion

### 3.1 Structural stability

Fig. 1 shows the enthalpy–pressure curves of  $\text{Ir}_2\text{P}$  for the  $I4/mmm$  phase relative to the  $Fm\bar{3}m$  phase. It indicates that the  $Fm\bar{3}m$  phase is most energetically favorable at ambient pressure. However, as pressure increases, the phase changes to the  $I4/mmm$  phase at 103.4 GPa. The crystal structures of  $\text{Ir}_2\text{P}$  are shown in Fig. 2. It can be observed that the  $Fm\bar{3}m$  and  $I4/mmm$  phase of  $\text{Ir}_2\text{P}$  consist of four and two formula units per unit cell,

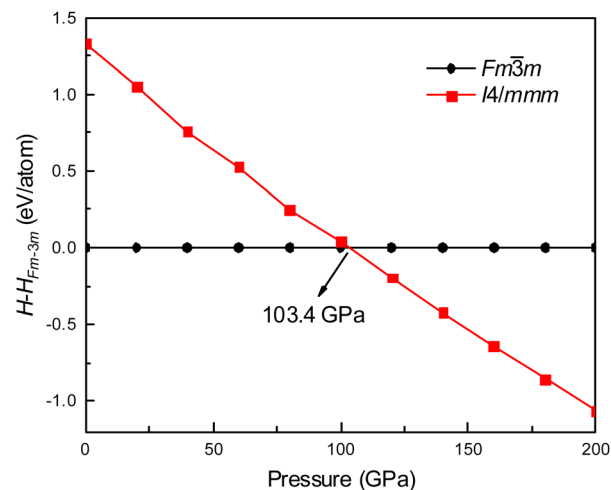


Fig. 1 Enthalpy–pressure curve of  $\text{Ir}_2\text{P}$  for  $I4/mmm$  phases relative to  $Fm\bar{3}m$  phase.

respectively. In the  $Fm\bar{3}m$  structure, the Ir atom is linked to the surrounding four P atoms to form the  $\text{IrP}_4$  tetrahedron, with an Ir–P bond length of 2.405 Å. In the  $I4/mmm$  structure, the two Ir atoms share four P atoms to form the  $\text{Ir}_2\text{P}_4$  regular octahedron, with an Ir–P bond length of 2.466 Å.

Several geometry optimizations were conducted using the LDA and GGA approximations. Fig. 3 shows the dependence of the calculated relative volume on the external pressure up to 80 GPa at zero temperature for  $\text{Ir}_2\text{P}$ . Previous studies have indicated that the pressure dependence of the volume ratio is a more direct measure of compressibility compared to the description of physical properties alone.<sup>34</sup> For comparison, the experimental and theoretical data up to 40.6 GPa provided by Wang *et al.*<sup>34</sup> are also plotted Fig. 3, along with the theoretical  $P$ – $V/V_0$  data of conventional superhard materials such as diamond and  $c$ -BN<sup>50</sup> at  $T = 0$  K up to 80 GPa. Our results obtained with DFT calculations match well with that of Wang *et al.*<sup>34</sup> Due to the discrepancy between GGA and LDA for exchange–correlation potentials within the DFT framework, the average

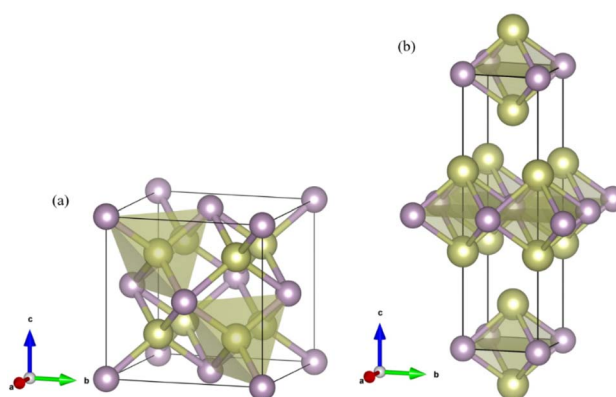


Fig. 2 Crystal structures for the (a)  $Fm\bar{3}m$  and (b)  $I4/mmm$  phases of  $\text{Ir}_2\text{P}$ . The gold and purple spheres represent Ir and P atoms, respectively.



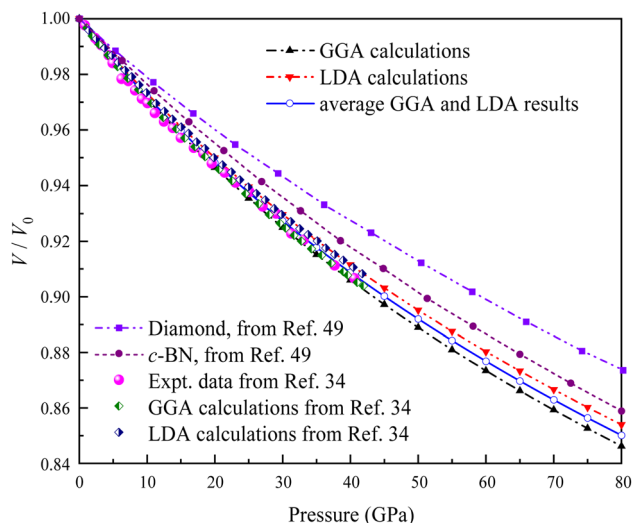


Fig. 3 Comparison of the calculated pressure versus volume ratio of 0 K isotherms for the anti-fluorite structure of  $\text{Ir}_2\text{P}$  with experiments and other theoretical data.

of GGA and LDA values is employed as the rescaled estimate. It is evident from Fig. 3 that the anti-fluorite structured  $\text{Ir}_2\text{P}$  is more compressible than conventional superhard materials, such as *c*-BN and diamond. This implies that the anti-fluorite structure may exhibit a higher degree of flexibility or less resistance to pressure, compared to the conventional superhard materials.

Table 1 lists the parameters of the fitted equation of state (EOS) for  $\text{Ir}_2\text{P}$  with the cubic anti-fluorite structure. These parameters include  $a_0$ ,  $V_0$ ,  $K_0$  and  $K'_0$ , which were obtained from the 3rd-order Birch–Murnaghan EOS<sup>51</sup> using the Eosfit52 software.<sup>52</sup> To analyze the results from EOS, we have also included the results from DFT and experiments by Wang *et al.*<sup>34</sup> in Table 1. Unfortunately, we cannot compare the results of equilibrium lattice parameter  $a_0$  and equilibrium volume  $V_0$  among studies due to the lack of data. However, the values of bulk modulus  $K_0$  and its first pressure derivative  $K'_0$  obtained from DFT calculations are in very good agreement with the theoretical results and are also comparable to the ones obtained from the X-ray diffraction experiment data of Wang *et al.*<sup>34</sup> This indicates that our calculations are accurate, and the methods can be used

**Table 1** The calculated equilibrium lattice constant  $a_0$ , equilibrium volume  $V_0$ , isothermal bulk modulus  $B_0$  and its pressure derivative  $K'_0$  from the 3rd-order Birch–Murnaghan equation for  $\text{Ir}_2\text{P}$  with the anti-fluorite structure compared with the experimental and other theoretical data

Method	$a_0$ (Å)	$V_0$ (Å <sup>3</sup> )	$B_0$ (GPa)	$K'_0$	
DFT-GGA	5.555	171.415	318.010	4.881	This work
DFT-LDA	5.483	164.828	343.879	4.895	This work
Average	5.519	168.122	330.945	4.888	This work
DFT-GGA			320	5.0	Ref. 34
DFT-LDA			342	5.0	Ref. 34
Experiment			306(6)	6.4(5)	Ref. 34

to predict other properties of  $\text{Ir}_2\text{P}$  with the anti-fluorite structure.

In order to better understand the structural stability of cubic  $\text{Ir}_2\text{P}$  under strain, it is important to calculate the elastic constants of the material. Table 2 presents the calculated elastic constants  $C_{11}$ ,  $C_{12}$ , and  $C_{44}$ ,  $G$ , Young's modulus ( $E$ ), and Poisson's ratio ( $\nu$ ) for  $\text{Ir}_2\text{P}$  with the anti-fluorite structure at zero pressure and zero temperature. The values for  $E$ ,  $G$ , and  $\nu$  are derived according to the Voigt–Reuss–Hill averaging scheme.<sup>53</sup> For any crystal to be mechanically stable, it must have a positive strain energy.<sup>54</sup> The elastic constants obtained suggest that the  $\text{Ir}_2\text{P}$  with anti-fluorite structure is mechanically stable. However, despite its elastic stability,  $\text{Ir}_2\text{P}$  with an anti-fluorite structure has smaller  $B$  (316.520 and 343.068 GPa), lower  $G$  (117.656 and 129.203 GPa), and larger  $\nu$  (0.335 and 0.333) when calculated using GGA and LDA in the DFT framework. This suggests that its mechanical properties are inferior in comparison to conventional superhard materials like diamond and *c*-BN.<sup>50</sup>

It is well-documented that GGA in first-principles calculations often overestimates volume and underestimates bulk modulus.<sup>55</sup> This shortcoming is also extended to the elastic constant calculations at high pressure, like  $C_{11}$ , for the *Fm* $\bar{3}$ *m* and *I4*/*mmm* phases of  $\text{Ir}_2\text{P}$ , as shown in Fig. 4. It is found that the effect of the pressure on  $C_{11}$  (679.459 and 1307.119 GPa for GGA and 739.766 and 1373.326 GPa for LDA calculations at 0 and 80 GPa, respectively), which represents elasticity in length, is much larger than that on  $C_{12}$  (135.050 and 360.009 GPa for GGA and 144.719 and 368.275 GPa for LDA calculations at 0 and 80 GPa, respectively) and  $C_{44}$  (61.741 and 117.102 GPa for GGA and 68.134 and 124.536 GPa for LDA calculations at 0 and 80 GPa, respectively), which characterize the elasticity in shape in the pressure range of 0–80 GPa. However, this little discrepancy in the presentation doesn't influence the judgment of the high-pressure structural stability for the cubic  $\text{Ir}_2\text{P}$ . The obtained elastic constants exhibited in Fig. 4(b) show that the *I4*/*mmm* phase satisfies the Born criteria for tetragonal crystal systems in the pressure range studied.

It is widely accepted that a stable crystalline structure requires all phonon frequencies to be positive at zero temperature. To ensure this stability, the phonon dispersion calculation has been performed within the finite displacement theory using the PHONOPY code for the *Fm* $\bar{3}$ *m* and *I4*/*mmm* phases at 0, 100 and 120, 200 GPa, respectively. As demonstrated in Fig. 5, there are no imaginary frequencies present in the entire Brillouin zone at the selected pressures. This finding indicates that both phases are dynamically stable, meaning that the material remains stable under the applied pressure conditions, as there are no negative phonon frequencies that would suggest an instability in the crystalline structure. The absence of imaginary phonon frequencies also confirms that the material's elastic properties are well-defined and robust, rendering it suitable for a wide range of applications.<sup>54</sup> The phonon spectra of the *Fm* $\bar{3}$ *m* and the *I4*/*mmm* phases are divided into two modes, low and high frequency modes. Both phases demonstrate notable phononic gaps within the frequency ranges of 6.3–9.9 THz and 8.2–11.9 THz, respectively, along the optical branch at 0 GPa and 120 GPa. These broader phononic gaps separate the optical



**Table 2** Calculated zero-pressure elastic constants  $C_{ij}$ , shear modulus  $G$ , Young's modulus  $E$ , and Poisson's ratio  $\nu$  for  $\text{Ir}_2\text{P}$  with the anti-fluorite structure

Method	$C_{11}$ (GPa)	$C_{12}$ (GPa)	$C_{44}$ (GPa)	$G$ (GPa)	$E$ (GPa)	$\nu$	
DFT-GGA	679.459	135.050	61.741	117.656	314.055	0.335	This work
DFT-LDA	739.766	144.719	68.134	129.203	344.377	0.333	This work

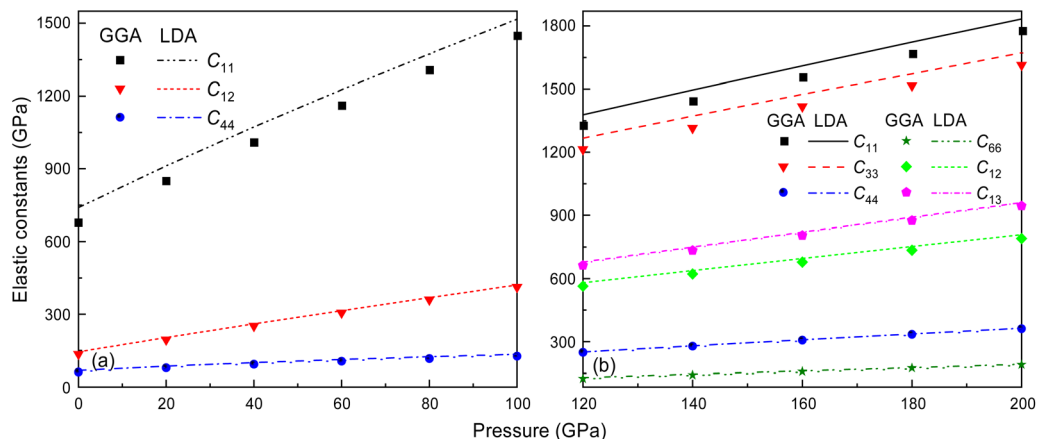


**Fig. 4** The calculated elastic constants for  $Fm\bar{3}m$  and  $I4/mmm$  phases of  $\text{Ir}_2\text{P}$  as a function of pressure at zero temperature. The dots and lines denote the results coming from GGA and LDA methods, respectively.

phonon modes into high and low-frequency modes. Moreover, both phases exhibit an increasing phononic gap with increasing pressure, with the value increasing from 3.6 (0 GPa) to 5.9 (100

GPa) for the  $Fm\bar{3}m$  phase and 3.7 (120 GPa) to 4 (200 GPa) for the  $I4/mmm$  phase. This finding suggests that  $\text{Ir}_2\text{P}$  hold potential as materials for phononic devices, including applications in

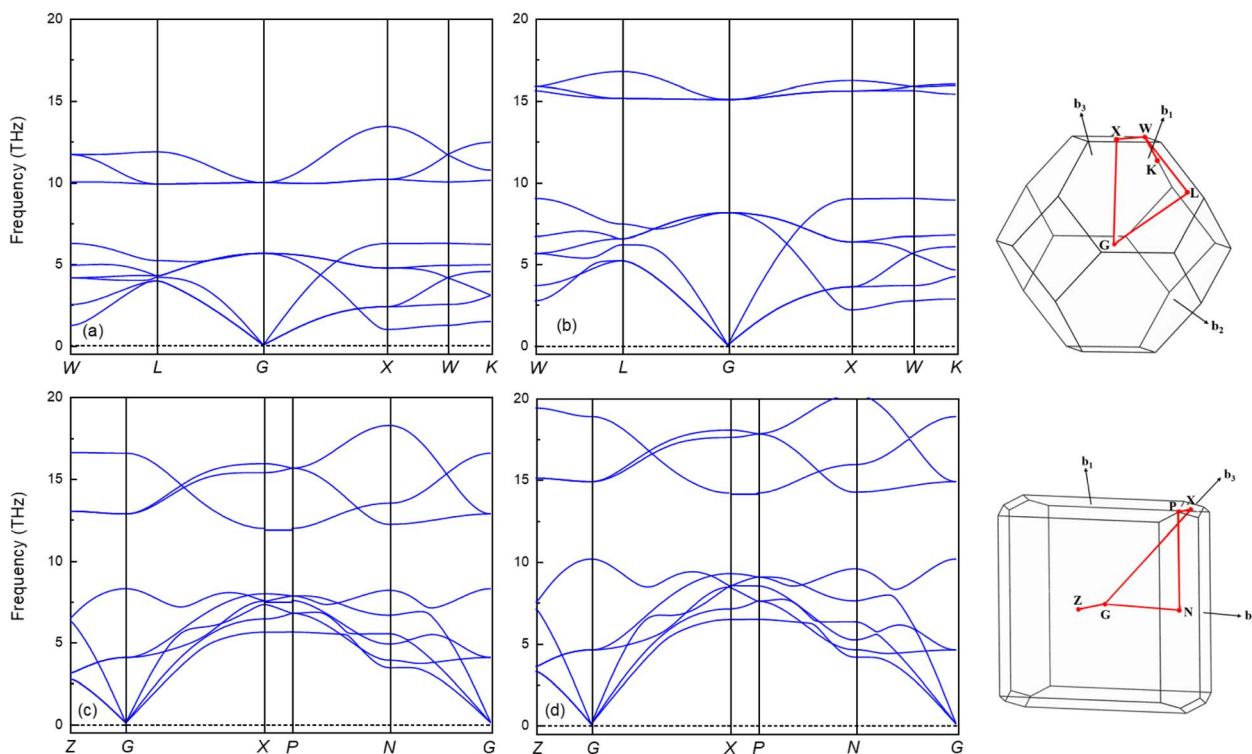


**Fig. 5** The calculated phonon dispersion curves of  $\text{Ir}_2\text{P}$  for  $Fm\bar{3}m$  at (a) 0 and (b) 100 GPa and  $I4/mmm$  phases at (c) 120 and (d) 200 GPa, respectively.



phonon waveguides, cavities, and filters.<sup>56–58</sup> Subsequently, the GGA with a correction of the Perdew–Burke–Ernzerhof version, the PBEsol, which is known to yield better results for solids, is used to investigate the electronic and finite-temperature thermodynamic properties of Ir<sub>2</sub>P with the anti-fluorite structure.

### 3.2 Electronic structure

The band structure and total density of states (TDOS) of *Fm* $\bar{3}$ *m* and *I4*/*mmm* with and without spin–orbit coupling (SOC) at 0 and 120 GPa are calculated to assess the potential impact of SOC, as shown in Fig. S3.† The results indicate that the band structure and TDOS near the Fermi level ( $E_F$ ) remains essentially unchanged with the inclusion of SOC, suggesting the weak influence of SOC in Ir<sub>2</sub>P. Fig. 6 and 7 show their band structure, TDOS and partial density of states (PDOS) without SOC. As shown in Fig. 6, the valence band of the *Fm* $\bar{3}$ *m* phase crosses the  $E_F$  and meets with the conduction band between the *G* and *X* points, while for the *I4*/*mmm* phase both the valence and conduction bands cross the  $E_F$ . The absence of an energy gap indicates metallic features for both structures, which is consistent with other results.<sup>33,34</sup> The calculated PDOS reveals that the Ir-d orbitals near the  $E_F$  play a leading role in the metallicity of both structures. Moreover, significant orbital hybridization below and above the  $E_F$  for P-p and Ir-d implies that there are strong interactions between P and Ir atoms. To further investigate their chemical bonding in detail, the electronic localization functions (ELF) of the *Fm* $\bar{3}$ *m* and *I4*/*mmm* phases in the (110) planes are subsequently calculated at 0 and 120 GPa, respectively, as illustrated in Fig. 7(e) and (f). In both phases, adjacent Ir atoms exhibit metallic bonding, as evidenced by the proximity of the ELF value to 0.5. Conversely, the electrons between neighboring P atoms exhibit high delocalization, signifying a non-bonded state, as indicated by an ELF value close to zero. The ELF analysis reveals the manifestation of polar covalent and metallic bonding between neighboring Ir

and P atoms. This is evident in the presence of a local maximum that distinctly favors the P atoms, with an ELF value of about 0.5 near the central region. Further Bader charge analysis reveals that, due to the electronegativity difference between Ir and P atoms in both *Fm* $\bar{3}$ *m* and *I4*/*mmm* phases, each P atom transfers a charge of 0.210e (0 GPa) and 0.265e (120 GPa) to the Ir atom, respectively. This charge transfer process substantiates the formation of ionic bonds between Ir and P atoms (see Table S1†). The analysis above reveals a multifaceted nature of the bond for both phases, encompassing ionic, covalent, and metallic components. Notably, the presence of covalent and ionic bonds contributes to structural stability and imparts excellent mechanical properties to the material. These findings show that Ir<sub>2</sub>P is a potential candidate for hard conductors in extreme conditions. With the pressure increase from 0 (120 GPa) to 100 GPa (200 GPa) for the *Fm* $\bar{3}$ *m* (*I4*/*mmm*) phase, the bond length among atoms in structures decrease monotonously. As a consequence, the number of charge transfers between Ir and P increases (see Table S1†), as shown in the band structure that conduction bands move up while valence bands move down. Furthermore, both structures are expected to have superconductivity because they both have steep and flat energy bands near  $E_F$  and high DOS values at  $E_F$ .

### 3.3 Superconductivity

The superconductivity of these two structures continues is being investigated based on their electronic structures. The EPC and  $T_c$  are calculated and presented in Table 3. The  $T_c$  decreases as pressure increases, with the value changing from 2.51 (*Fm* $\bar{3}$ *m* at 0 GPa) to 0.83 K (*I4*/*mmm* at 200 GPa). To understand the change in superconductivity, the projected phonon densities of states (PHDOS), Eliashberg phonon spectral function  $\alpha^2F(\omega)$  and integrated electron-phonon coupling  $\lambda(\omega)$  of the Ir<sub>2</sub>P at 0 and 200 GPa are analyzed, as seen Fig. 8. The PHDOS for the *Fm* $\bar{3}$ *m* and *I4*/*mmm* phases reveal that their high-frequency

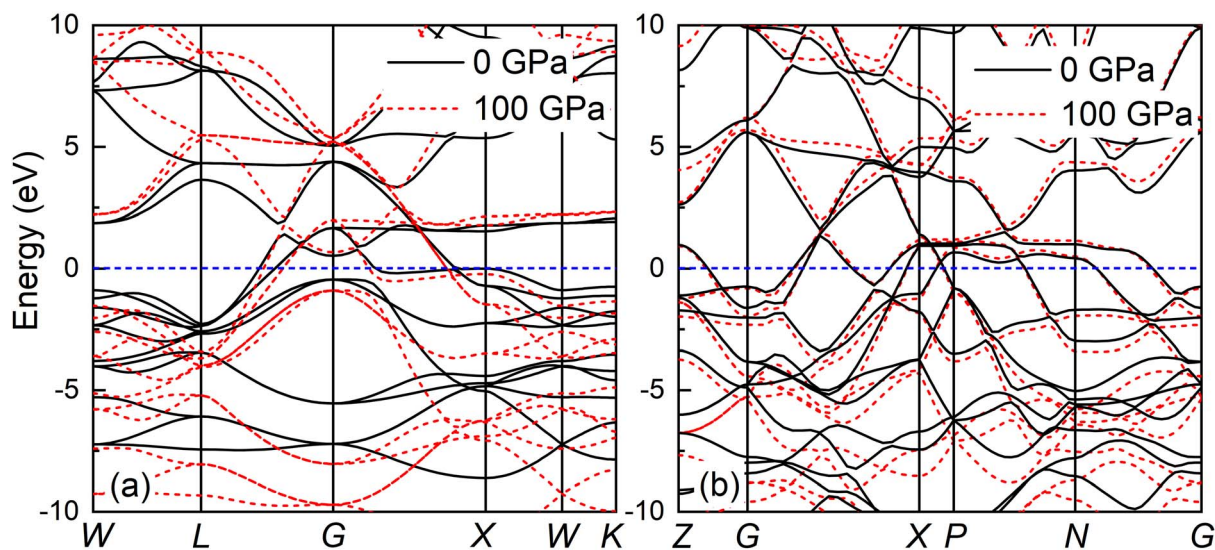


Fig. 6 Band structures of (a) *Fm* $\bar{3}$ *m* phase at 0 and 100 GPa and (b) *I4*/*mmm* phase at 120 and 200 GPa for Ir<sub>2</sub>P calculated using GGA with Fermi energy level taken at 0 eV, as shown by the short blue dash line.

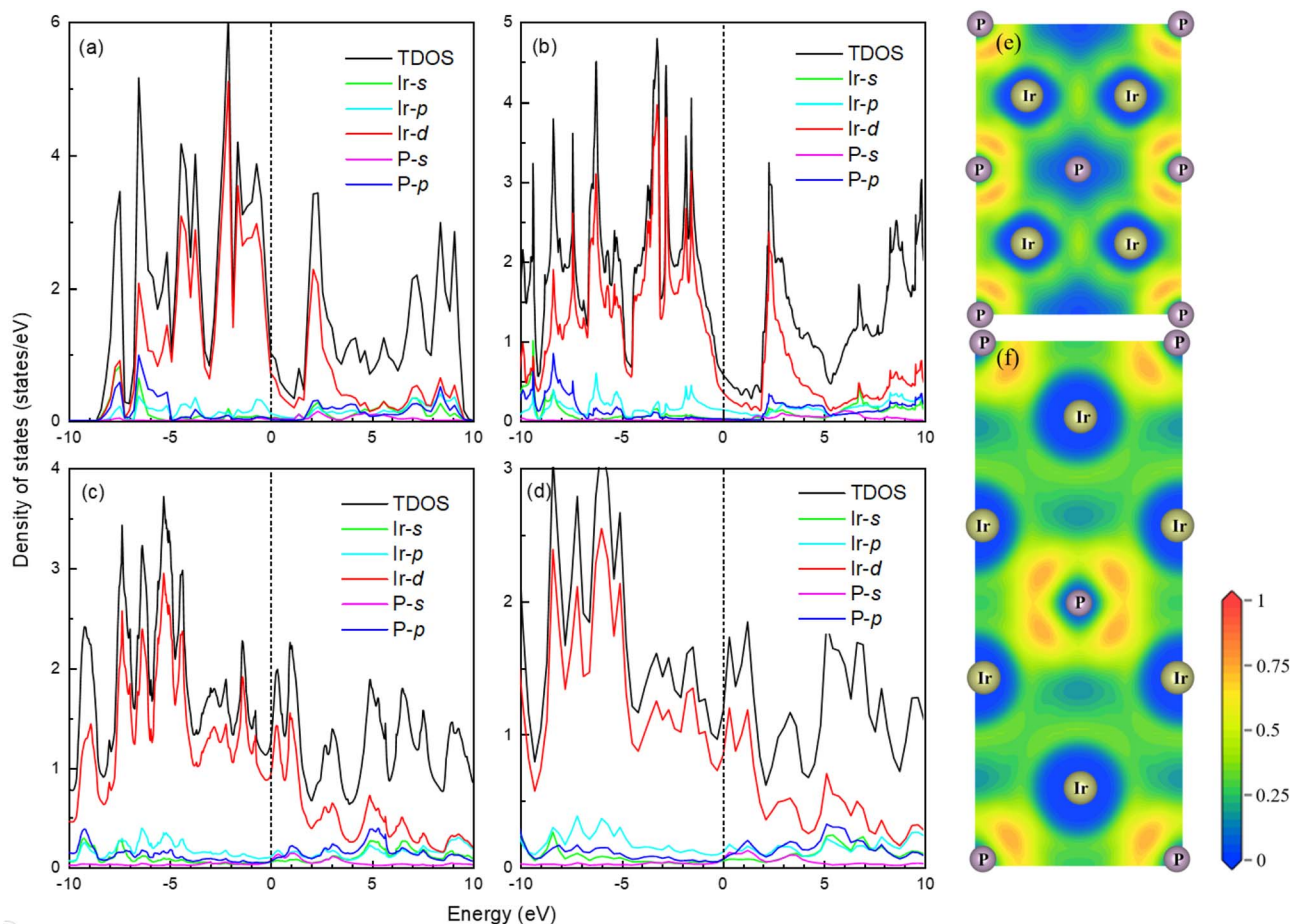


Fig. 7 The total and partial density of states of  $Fm\bar{3}m$  phase at (a) 0 and (b) 100 GPa as well as  $I4/mmm$  phase at (c) 120 and (d) 200 GPa for  $Ir_2P$  from GGA calculations with Fermi energy level taken at 0 eV, as shown by the short blue dash line. The electronic local functions of the  $Fm\bar{3}m$  and  $I4/mmm$  phases in (110) planes at (e) 0 and (f) 120 GPa, respectively.

**Table 3** The calculated density of states at Fermi level  $N_{EF}$  (electrons/eV), electron-phonon coupling parameter  $\lambda$ , logarithmic average phonon frequency  $\omega_{log}$  (K) and superconducting critical temperature  $T_c$  (K) of the  $Fm\bar{3}m$  and  $I4/mmm$  at different pressure (GPa)

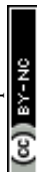
Phase	Pressure	$N_{EF}$	$\lambda$	$\omega_{log}$	$T_c$ ( $\mu^*$ = 0.1)	$T_c$ ( $\mu^*$ = 0.13)
$Fm\bar{3}m$	0	0.91	0.63	94.00	2.51	1.83
$I4/mmm$	200	0.95	0.38	283.71	0.89	0.35

modes are both associated with the vibrations of P atoms. The low-frequency modes of the former are connected to the vibrations of Ir atoms, while the latter are linked to the coupling of Ir and P atoms. This observation indicates that the phononic gaps displayed in Fig. 5 in both phases arise from the significant mass disparity between the heavy Ir atoms and the lighter P atoms. The relevant parameters are listed in Table 3. For  $Fm\bar{3}m$  phase, the  $\lambda$  and the  $\omega_{log}$  are 0.63 and 94 K at 0 GPa. From the PHDOS and Eliashberg phonon spectral function  $\alpha^2F(\omega)$  as well as integrated electron-phonon coupling  $\lambda(\omega)$  presented in the left panel of Fig. 8, it is clear that the total  $\lambda$  is mainly donated by

the Ir atoms, P atoms by only 8%. In comparison, the  $I4/mmm$  phase at 200 GPa has a larger  $\omega_{log}$  with a value of 283.7 K, while  $\lambda$  decreases to 0.38. In combination with the electronic structures of both structures [Fig. 7(a) and (d)], one can find that a key factor for small  $\lambda$  is PDOS of Ir atoms at the  $E_F$ , which weakens the  $T_c$  in  $I4/mmm$  compared to the  $Fm\bar{3}m$  phase. Specifically, the pressure facilitates charge transfer from Ir to P atoms in the  $I4/mmm$  phase at 200 GPa when comparing to  $Fm\bar{3}m$  at 0 GPa. As a consequence, the PDOS of Ir atoms at the  $E_F$  decrease [Fig. 7(a) and (d)], which strengthens the Ir–P bonds, and thus enhances the Ir–P vibration coupling, as shown in PHDOS for  $I4/mmm$  and  $Fm\bar{3}m$  phase presented in Fig. 8. The resulting smaller  $\lambda$  decreases the  $T_c$ .

### 3.4 Optical properties

The optical properties of both phases of  $Ir_2P$  have been studied by calculating the variation of the dielectric function  $\epsilon_1(\omega)$  and  $\epsilon_2(\omega)$  with energy at different pressures. The outcomes for the low-energy and high-energy regions are depicted in Fig. 9 and S4,† respectively. Both phases exhibit Drude behavior, which is a characteristic feature of metallic systems, as indicated by substantial negative values of  $\epsilon_1(\omega)$  in the low-energy range



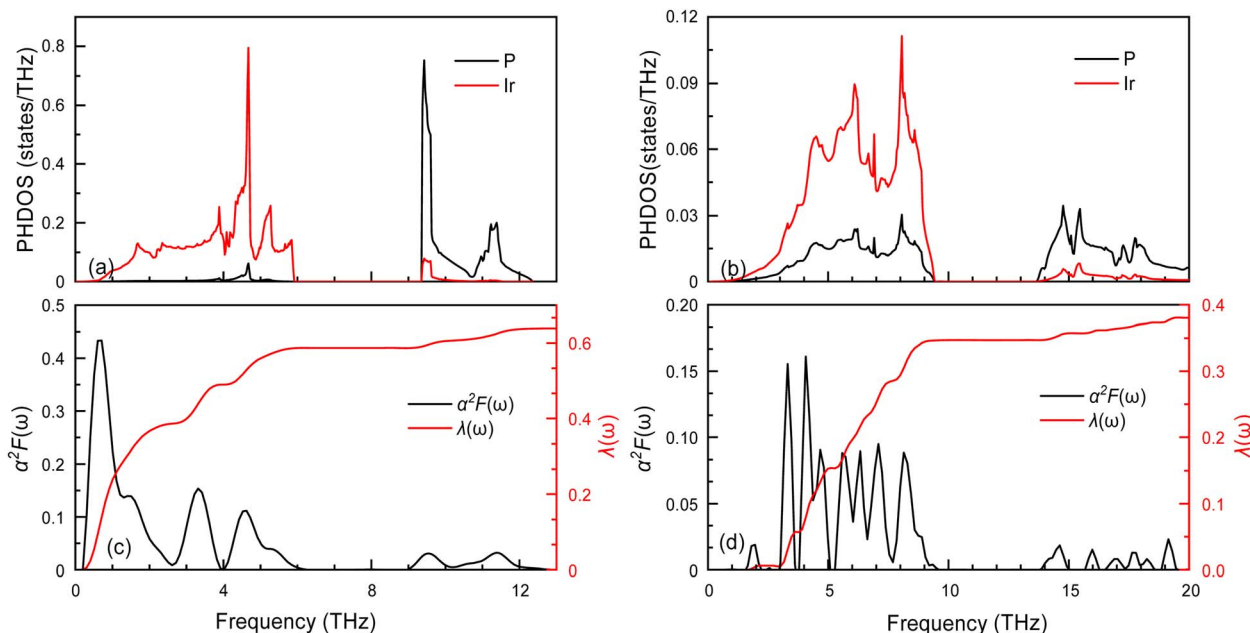


Fig. 8 The projected phonon densities of states PHDOS, Eliashberg phonon spectral function  $\alpha^2F(\omega)$  and integrated electron-phonon coupling  $\lambda(\omega)$  of the (a) and (c)  $Fm\bar{3}m$  and (b) and (d)  $I4/mmm$ .

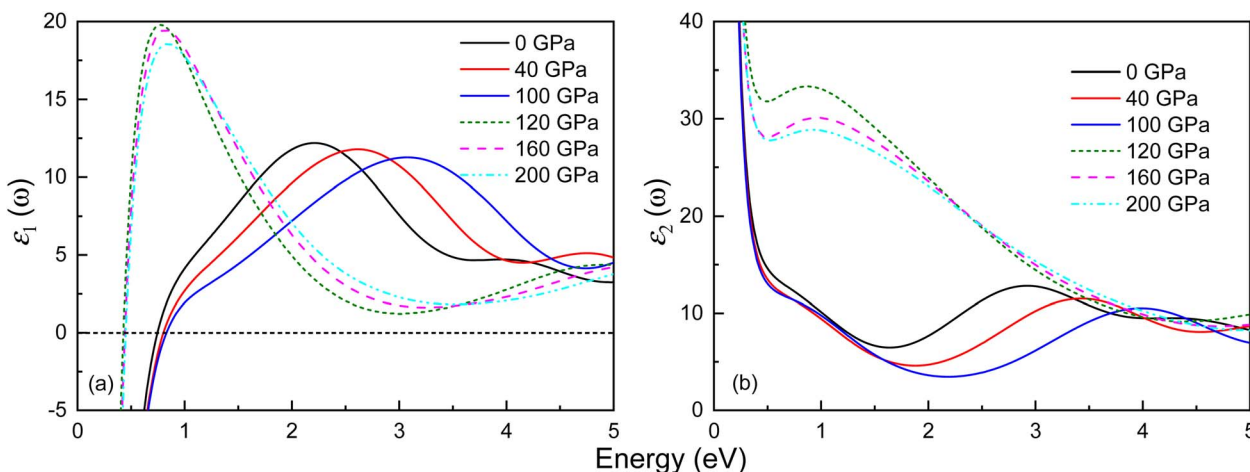


Fig. 9 Energy dependence of the (a) real part  $\varepsilon_1(\omega)$  and (b) imaginary part  $\varepsilon_2(\omega)$  of the complex dielectric function for the  $Fm\bar{3}m$  and  $I4/mmm$  phases of  $Ir_2P$  at different pressures. The solid and dashed lines represent the  $Fm\bar{3}m$  and  $I4/mmm$  phases, respectively.

below 1 eV. Their  $\varepsilon_1(\omega)$  curves show a general trend of increasing and then decreasing with rising energy. In the high-energy region, their values become negative, signifying that the material behaves opaquely (see Fig. S4†). All observable peaks of  $\varepsilon_2(\omega)$  are within the energy range of 0–5 eV, and above 20 eV, the value of  $\varepsilon_2(\omega)$  tends to zero. The  $\varepsilon_2(\omega)$  curves of the  $Fm\bar{3}m$  and  $I4/mmm$  phases exhibit peaks at 2.93 and 0.88 eV at 0 and 120 GPa, respectively. Their shift of  $\varepsilon_2(\omega)$  towards the high-energy region, indicating a blueshift, with increasing pressure, is associated with the enhancement of electron transition at high pressure.

Fig. 10 and S5† display the optical properties of  $Ir_2P$  under pressure in the low-energy and high-energy regions, including the absorption coefficient  $\alpha(\omega)$ , reflectivity  $R(\omega)$ , optical

conductivity  $\sigma(\omega)$ , and loss function  $L(\omega)$ . The starting point of optical absorption coefficient at zero photon energy indicates that  $Ir_2P$  has metallicity, which is consistent with its electronic structures (see Fig. 6 and 7). In Fig. 10(a) and S5,† the optical absorption spectra of both structures show a broad, continuous absorption characteristic, distinct from the well-defined absorption peaks in semiconductors or insulators. This is attributed to the continuous band structure of metallic materials, lacking a band gap, which allows electrons to move freely, leading to a more uniform absorption of light. The presence of these inconspicuous absorption peaks is associated with electron transition, as incident light imparts energy to electrons, prompting their transition from the ground state to the excited



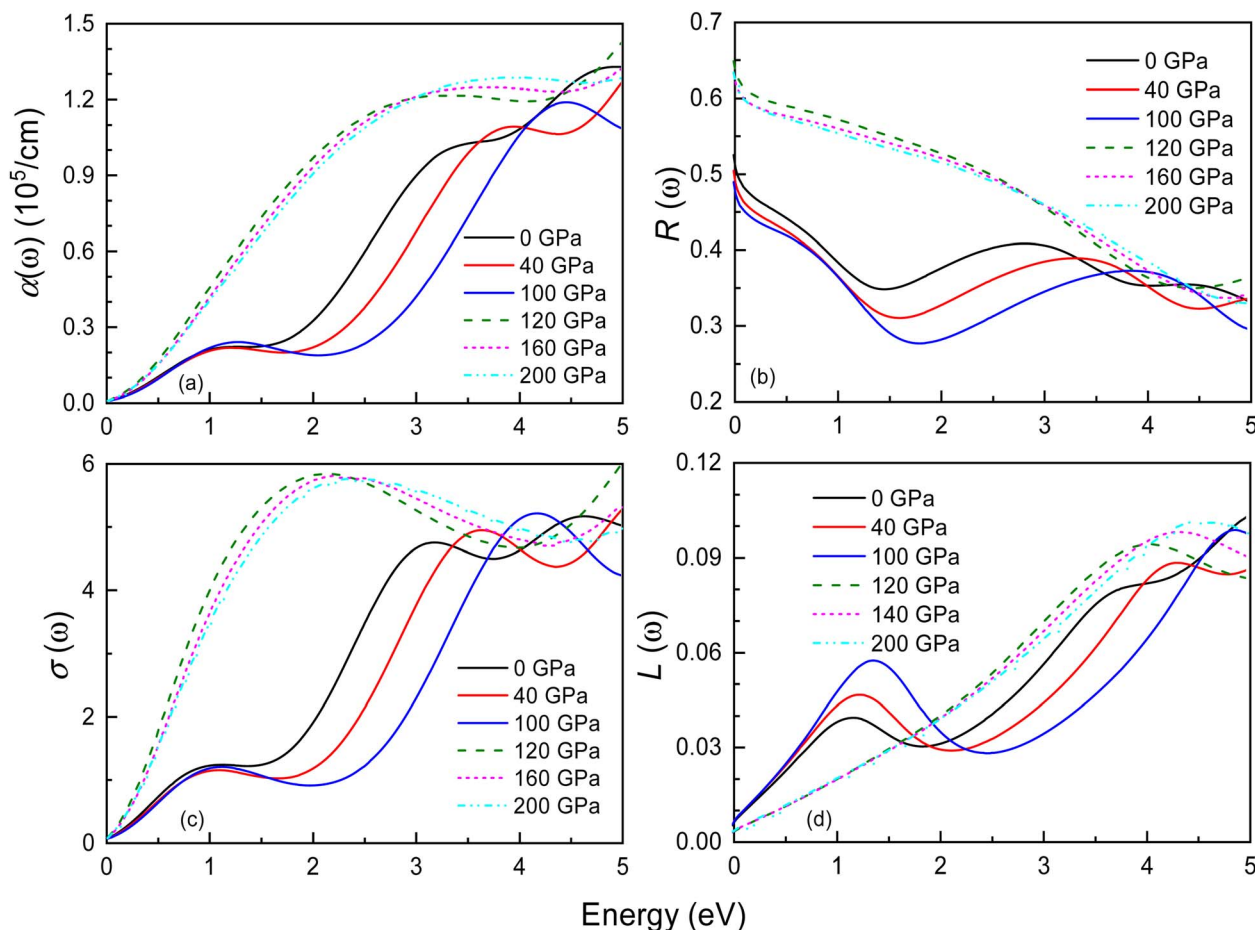


Fig. 10 Energy dependence of the (a) absorption coefficient  $\alpha(\omega)$ , (b) reflectance  $R(\omega)$ , (c) optical conductivity  $\sigma(\omega)$ , and (d) loss function  $L(\omega)$  for the  $Fm\bar{3}m$  and  $I4/mmm$  phases of  $\text{Ir}_2\text{P}$  at different pressures. The solid and dashed lines represent the  $Fm\bar{3}m$  and  $I4/mmm$  phases, respectively.

state. Additionally, their values progressively rise with energy, peaking at 14.9 (0 GPa) and 15.4 eV (120 GPa), respectively, implying the materials' proficiency as ultraviolet absorbers. Their overall absorption region and peaks exhibit an increase with rising pressure. These findings suggest that applying pressure can broaden the photoresponse range of  $\text{Ir}_2\text{P}$  and improve its light absorption in the ultraviolet region [see Fig. S5(a)†]. Both structures exhibit reflectivity values exceeding 76% in the 25–35 eV, suggesting that  $\text{Ir}_2\text{P}$  can serve effectively as a reflective coating within this energy range [see Fig. S5(b)†]. With increasing energy, their optical conductivity initiates an ascent from a photon energy of zero, attributed to the absence of a bandgap in  $\text{Ir}_2\text{P}$ , and culminates in a maximum in the ultraviolet region [see Fig. 10(c) and S5(c)†]. The research reveals that  $\text{Ir}_2\text{P}$  exhibits optical conductivity across the infrared, visible, and ultraviolet wavelength ranges. Based on Fig. 10(d) and S5(d),† it is evident that the  $Fm\bar{3}m$  and  $I4/mmm$  phases exhibit smaller loss function in the visible region, and their maximum energy loss peaks occur at 26.2 eV (0 GPa) and 31.3 eV (120 GPa), corresponding to their plasmonic frequencies, respectively. When the incident photon energy surpasses its plasma frequency, the absorption coefficient and reflectivity decrease drastically, and the  $\text{Ir}_2\text{P}$  becomes transparent,

implying that the  $\text{Ir}_2\text{P}$  changes from a metal response to a dielectric response. Moreover, both structures exhibit a blue-shift in reflectivity, optical conductivity and loss function with increasing pressure towards the high-energy region.

### 3.5 Thermodynamic properties

Thermodynamic quantities for the  $Fm\bar{3}m$  structure of  $\text{Ir}_2\text{P}$  at different pressures and temperatures have been obtained using the QHD model. The calculated energy-volume points at zero temperature and pressure are used to generate the results shown in Fig. 11. The volume curves become steeper with increasing temperature, indicating that the anti-fluorite structure of  $\text{Ir}_2\text{P}$  is more easily compressed under higher temperatures. The isothermal bulk modulus  $B$  increases with increasing pressure but generally decreases with rising temperature when looking at the overall trend of the results (Fig. 11). Upon careful examination, it is discovered that  $B$  slightly and linearly decreases with temperature at a constant pressure, and increases with pressure at a fixed temperature. This is consistent with the volume expansion trend. These findings suggest that pressure has a more significant impact on  $B$  than temperature for  $\text{Ir}_2\text{P}$ .



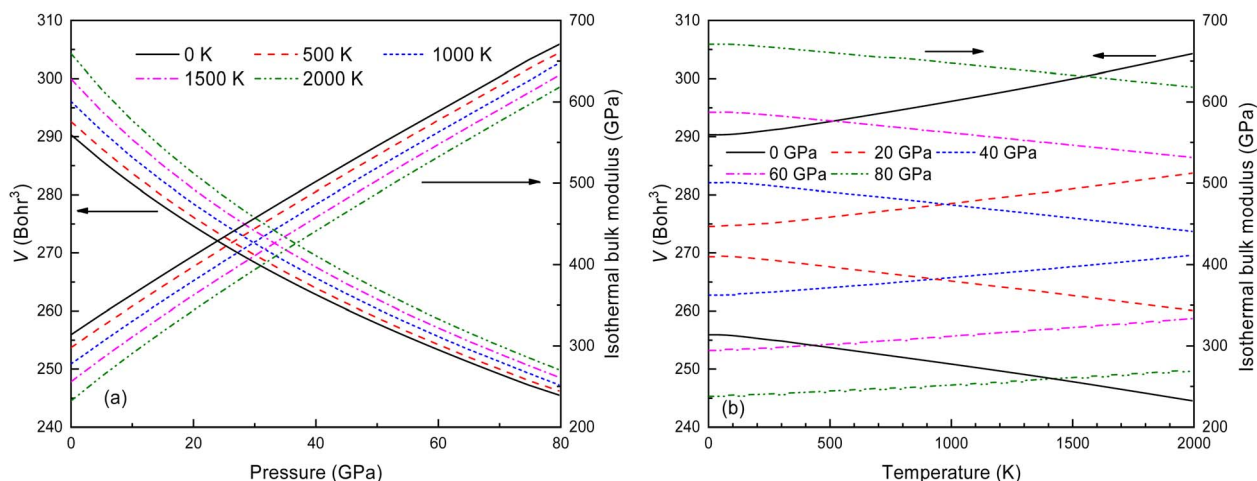


Fig. 11 The calculated volume and bulk modulus for the  $Fm\bar{3}m$  phase of  $\text{Ir}_2\text{P}$  (a) as a function of pressure at different temperatures and (b) as a function of temperatures at various pressures.

The  $B$  value of  $\text{Ir}_2\text{P}$  changes regularly with temperature and pressure. However, the first and second pressure derivatives of  $B$ ,  $B'_T$  and  $B''_T$  show some variation with changes in pressure and temperature, as shown in Fig. 12. Li *et al.*<sup>59</sup> noted that the  $B'_T$  and  $B''_T$  derived from the three-parameter Vinet or Rose EOS often deviate significantly from experimental observations, indicating the need for further development of the EOS with improved performance. As shown in Fig. 12(a) and (b),  $B'_T$  increases with the temperature throughout the pressure range of 0–80 GPa, while  $B''_T$  decreases rapidly at low pressures, and moderately at higher pressures with an increase in temperature. For  $\text{Ir}_2\text{P}$ , reducing pressure has a similar effect on  $B'_T$  as increasing temperature. When the pressure is less than 30 GPa,  $B''_T$  changes sharply, and gradually becomes gentler with an increase in pressure, remaining relatively stable after the pressure exceeds 40 GPa. Therefore, under high-pressure conditions, the response of  $B''_T$  in  $\text{Ir}_2\text{P}$  to temperature change is relatively slow.

In the quasi-harmonic approximation, anharmonicity is limited to thermal expansion. Fig. 13 shows how the volume thermal expansion coefficient  $\alpha$  changes with temperature under different pressures. As seen in Fig. 13(a) and (b),  $\alpha$  decreases significantly with increasing pressure at various temperatures, and increases with rising temperature at different pressures. This indicates that anharmonic effects have a significant impact on the antifluorite structure of  $\text{Ir}_2\text{P}$  under low-pressure and high-temperature conditions.

Fig. 14 illustrates the relationship between the Debye temperature, pressure and temperature for  $\text{Ir}_2\text{P}$  with the antifluorite structure. As displayed in Fig. 14(a) and (b), it can be observed that  $\theta_D$  values increase with the rise in pressure. At low pressures, the  $\theta_D$  value undergoes a significant reduction when the temperature varies from 0 to 2000 K. Nonetheless, as the pressure increases, the extent of this reduction becomes less significant. To the best of our knowledge, this is the first quantitative theoretical prediction for  $\text{Ir}_2\text{P}$  concerning the

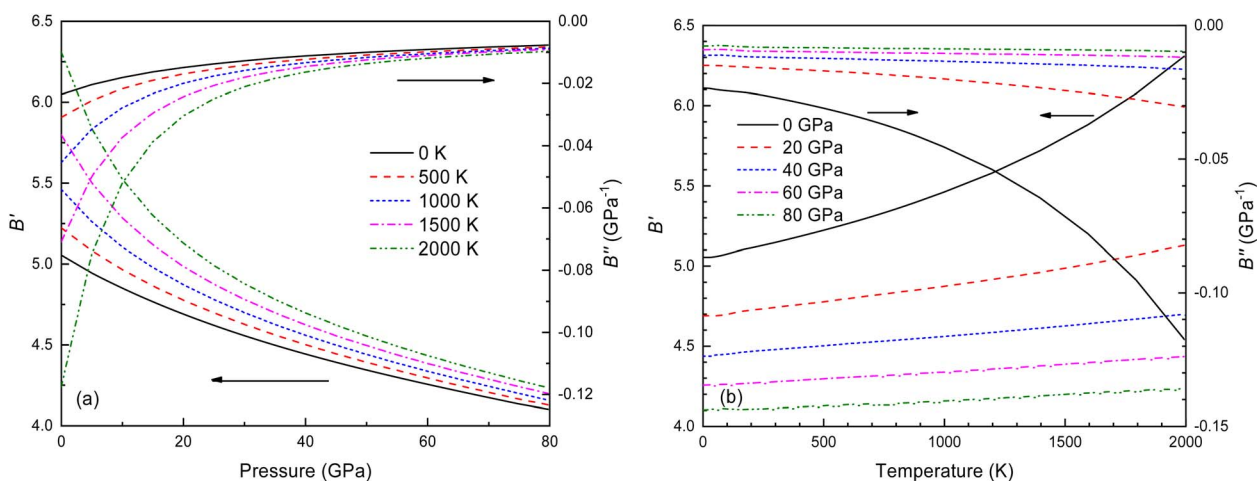


Fig. 12 (a) Pressure dependence of the  $B'_T$  and  $B''_T$  at different temperatures and (b) temperature dependence of the  $B'_T$  and  $B''_T$  at various pressures for  $Fm\bar{3}m$  phase of  $\text{Ir}_2\text{P}$ .

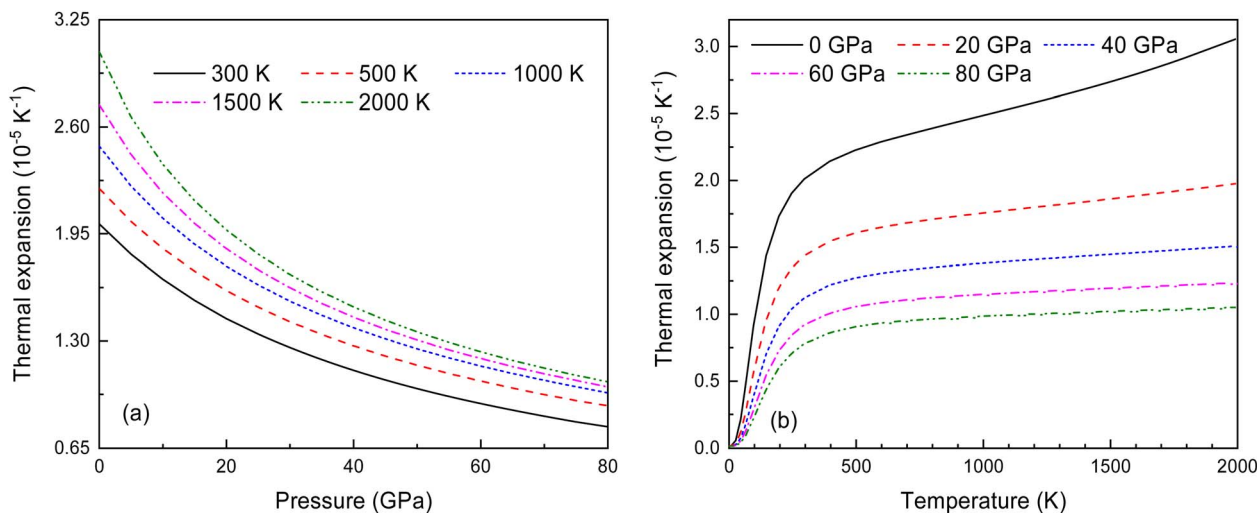


Fig. 13 (a) The pressure-dependent thermal expansion coefficient  $\alpha$  at various temperatures and (b) the temperature-dependent  $\alpha$  at various pressures for  $Fm\bar{3}m$  phase of  $Ir_2P$ .

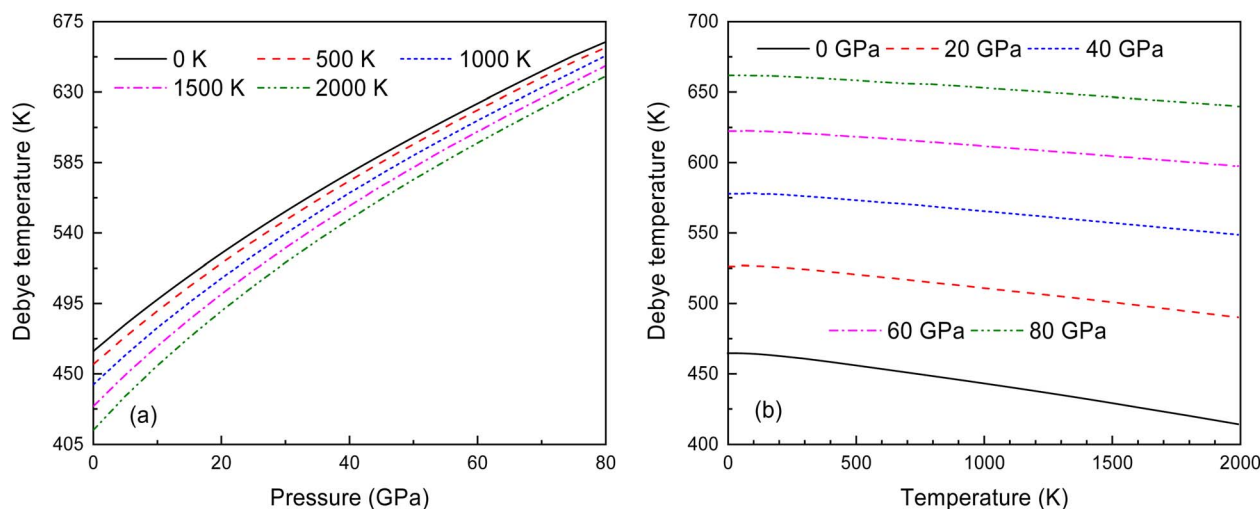


Fig. 14 (a) Pressure dependence of the  $\theta_D$  at various temperatures and (b) temperature dependence of  $\theta_D$  at various pressures for  $Fm\bar{3}m$  phase of  $Ir_2P$ .

pressure and temperature dependence of the Debye temperature. Further research is needed to experimentally confirm these findings.

## 4. Conclusions

First-principles calculations and the quasi-harmonic approximation were employed to examine the ground-state characteristics and the elastic, electronic, and finite-temperature thermodynamic properties of  $Ir_2P$  as a function of pressure and temperature. The study found that the GGA is more suitable than the LDA for describing the ground-state properties of  $Ir_2P$ . Good agreement has been achieved with existing experimental and theoretical studies, indicating that the GGA provides a more accurate representation of the material's properties. The analysis of the calculated results indicates that the anti-fluorite

structure of  $Ir_2P$  is a potential candidate for being one of the hard materials. With further increase in pressure, the  $Fm\bar{3}m$  phase changes to the  $I4/mmm$  phase at 103.4 GPa. The mechanical and dynamical stabilities of  $Ir_2P$  in the studied pressure range are verified by the calculated elastic constants and phonon dispersion curves. The electronic structure and EPC reveal that the  $Fm\bar{3}m$  and  $I4/mmm$  phases of  $Ir_2P$  are superconducting materials with  $T_c$  of 2.51 and 0.89 K at 0 and 200 GPa, respectively. Calculated optical properties show that both the  $Fm\bar{3}m$  and  $I4/mmm$  phases of  $Ir_2P$  are photoconductive in the infrared, visible, and ultraviolet regions. More interestingly, both the  $Fm\bar{3}m$  and  $I4/mmm$  phases of  $Ir_2P$  have reflectance higher than 76% in the energy range of 25–35 eV at different pressures, which suggests that both materials can be used as reflective coatings. The pressure and temperature dependencies of the primitive-cell volume,  $\theta_D$ ,  $B$ ,  $B'_T$ ,  $B''_T$ , and



$\alpha$  of  $Fm\bar{3}m$  phase were also evaluated within the ranges of 0–80 GPa and 0–2000 K using the QHD model. The fluctuation of  $B'_T$  and  $B''_T$ , which hold a crucial position in developing approximate EOS, has been forecasted for the anti-fluorite structure of  $\text{Ir}_2\text{P}$  within an expanded pressure and temperature range. The outcomes showed that the two parameters do not reach constant values as presumed in the EOS exploration at high pressures and temperatures. Here, the  $B'_T$  escalates with the rise in temperature, and the impact of declining pressure is equivalent to that of increasing temperature. Furthermore, for  $\text{Ir}_2\text{P}$ , the  $B''_T$  at high pressures is a weak function of temperature. Our calculations show that  $\text{Ir}_2\text{P}$  is a hard multifunctional material with superconductivity and excellent photoconductivity and reflectivity.

## Conflicts of interest

The authors declare that they have no known competing financial interests or personal relationships that could have appeared to influence the work reported in this paper.

## Acknowledgements

This study was supported by the Key Natural Science Foundation of Gansu Province (No. 20JR5RA427).

## References

- 1 K. Zhao, Q. Wang, W. Li, Q. Yang, H. Yu, F. Han, H. Liu and S. Zhang, *Phys. Rev. B*, 2022, **105**, 094104.
- 2 S. Liu, D. Xu, R. Liu, Z. Yao and P. Wang, *Dalton Trans.*, 2023, **52**, 1000–1008.
- 3 S. B. Schneider, D. Baumann, A. Salamat, Z. Konôpková, H.-P. Liermann, M. R. Schwarz, W. Morgenroth, L. Bayarjargal, A. Friedrich, B. Winkler and W. Schnick, *Chem. Mater.*, 2012, **24**, 3240–3246.
- 4 Z. Zhao, K. Bao, D. Li, D. Duan, F. Tian, X. Jin, C. Chen, X. Huang, B. Liu and T. Cui, *Sci. Rep.*, 2014, **4**, 4797.
- 5 R. W. Cumberland, M. B. Weinberger, J. J. Gilman, S. M. Clark, S. H. Tolbert and R. B. Kaner, *J. Am. Chem. Soc.*, 2005, **127**, 7264–7265.
- 6 B. Petermüller, C. Neun, K. Wurst, L. Bayarjargal, D. Zimmer, W. Morgenroth, M. Avalos-Borja, I. G. Becerril-Juarez, M. J. Mühlbauer, B. Winkler and H. Huppertz, *Inorg. Chem.*, 2018, **57**, 10341–10351.
- 7 Y. Wang, J. Zhang, L. L. Daemen, Z. Lin, Y. Zhao and L. Wang, *Phys. Rev. B: Condens. Matter Mater. Phys.*, 2008, **78**, 224106.
- 8 M. Xie, R. Mohammadi, Z. Mao, M. M. Armentrout, A. Kavner, R. B. Kaner and S. H. Tolbert, *Phys. Rev. B*, 2012, **85**, 064118.
- 9 E. Bykova, S. V. Ovsyannikov, M. Bykov, Y. Yin, T. Fedotenko, H. Holz, S. Gable, B. Merle, S. Chariton, V. B. Prakapenka, N. Dubrovinskaia, A. F. Goncharov and L. Dubrovinsky, *J. Mater. Chem. A*, 2022, **10**, 20111–20120.
- 10 W. Sun, X. Kuang, H. Liang, X. Xia, Z. Zhang, C. Lu and A. Hermann, *Phys. Chem. Chem. Phys.*, 2020, **22**, 5018–5023.
- 11 S. Khandarkhaeva, T. Fedotenko, M. Bykov, E. Bykova, S. Chariton, P. Sedmak, K. Glazyrin, V. Prakapenka, N. Dubrovinskaia and L. Dubrovinsky, *Eur. J. Inorg. Chem.*, 2020, **2020**, 2186–2190.
- 12 F. Kawamura, Y. Shibazaki, H. Yusa and T. Taniguchi, *Cryst. Growth Des.*, 2023, **23**, 2504–2510.
- 13 T. Sasaki, T. Yamamoto, S. Asano, K. Niwa and M. Hasegawa, *Dalton Trans.*, 2023, **52**, 469–475.
- 14 Y. Jin, W. Huang, J. Zhang, S. Li, S. Cheng, W. Sun, M. Ju and C. Zhang, *Arabian J. Chem.*, 2023, **16**, 104546.
- 15 C. Cui, J. Bi and C. Lu, *Cryst. Growth Des.*, 2022, **22**, 6201–6206.
- 16 R. Zhang, D. Legut, Z. Lin, Y. Zhao, H. Mao and S. Veprek, *Phys. Rev. Lett.*, 2012, **108**, 255502.
- 17 K. Zhao, Q. Wang, W. Li, Q. Yang, H. Yu, F. Han, H. Liu and S. Zhang, *Phys. Rev. B*, 2022, **105**, 094104.
- 18 X.-W. Sun, Q.-F. Chen, X.-R. Chen, L.-C. Cai and F.-Q. Jing, *J. Appl. Phys.*, 2011, **110**, 103507.
- 19 Y. Liang, J. Yang, L. Xi, C. Liu, G. Zhang and W. Zhang, *Mater. Today Phys.*, 2018, **7**, 54–60.
- 20 Y. Liang, C. Li, W. Guo and W. Zhang, *Phys. Rev. B: Condens. Matter Mater. Phys.*, 2009, **79**, 024111.
- 21 M. Kavitha, G. Sudha Priyanga, R. Rajeswarapalanichamy and K. Iyakutti, *J. Phys. Chem. Solids*, 2015, **77**, 38–49.
- 22 Y. Li, Y. Gao, B. Xiao, T. Min, Z. Fan, S. Ma and L. Xu, *J. Alloys Compd.*, 2010, **502**, 28–37.
- 23 Q. Wei, C. Zhao, M. Zhang, H. Yan and B. Wei, *Phys. Lett. A*, 2019, **383**, 2429–2435.
- 24 X. Jiang, Q. Xiong, S. Nam, F. Qian, Y. Li and C. M. Lieber, *Nano Lett.*, 2007, **7**, 3214–3218.
- 25 K. Y. Yoon, Y. Jang, J. Park, Y. Hwang, B. Koo, J.-G. Park and T. Hyeon, *J. Solid State Chem.*, 2008, **181**, 1609–1613.
- 26 A.-M. Alexander and J. S. Hargreaves, *Chem. Soc. Rev.*, 2010, **39**, 4388–4401.
- 27 P. Liu and J. A. Rodriguez, *J. Am. Chem. Soc.*, 2005, **127**, 14871–14878.
- 28 Y. Shi and B. Zhang, *Chem. Soc. Rev.*, 2016, **45**, 1529–1541.
- 29 R. H. Bowker, M. C. Smith, B. A. Carrillo and M. E. Bussell, *Top. Catal.*, 2012, **55**, 999–1009.
- 30 W. Blatz, F. Weibke and E. May, *Z. Anorg. Allg. Chem.*, 1935, **223**, 129–143.
- 31 S. Rundqvist, *Nature*, 1960, **185**, 31–32.
- 32 C. J. Raub, W. Zachariasen, T. Geballe and B. Matthias, *J. Phys. Chem. Solids*, 1963, **24**, 1093–1100.
- 33 C. M. Sweeney, K. L. Stamm and S. L. Brock, *J. Alloys Compd.*, 2008, **448**, 122–127.
- 34 P. Wang, Y. Wang, L. Wang, X. Zhang, X. Yu, J. Zhu, S. Wang, J. Qin, K. Leinenweber, H. Chen, D. He and Y. Zhao, *Sci. Rep.*, 2016, **6**, 21787.
- 35 X. Li, X. Ma, W. Gao and Y. Liu, *Chin. J. High Pressure Phys.*, 2019, **33**, 011103.
- 36 G. Kresse and J. Furthmüller, *Phys. Rev. B: Condens. Matter Mater. Phys.*, 1996, **54**, 11169.
- 37 D. Vanderbilt, *Phys. Rev. B: Condens. Matter Mater. Phys.*, 1990, **41**, 7892.



- 38 J. P. Perdew, A. Ruzsinszky, G. I. Csonka, O. A. Vydrov, G. E. Scuseria, L. A. Constantin, X. Zhou and K. Burke, *Phys. Rev. Lett.*, 2008, **100**, 136406.
- 39 J. P. Perdew and A. Zunger, *Phys. Rev. B: Condens. Matter Mater. Phys.*, 1981, **23**, 5048.
- 40 H. J. Monkhorst and J. D. Pack, *Phys. Rev. B: Solid State*, 1976, **13**, 5188.
- 41 T. H. Fischer and J. Almlof, *J. Phys. Chem.*, 1992, **96**, 9768.
- 42 L. Fast, J. Wills, B. Johansson and O. Eriksson, *Phys. Rev. B*, 1995, **51**, 17431.
- 43 C. Asker, L. Vitos and I. A. Abrikosov, *Phys. Rev. B: Condens. Matter Mater. Phys.*, 2009, **79**, 214112.
- 44 G. Grimvall, B. Magyari-Köpe, V. Ozoliņš and K. A. Persson, *Rev. Mod. Phys.*, 2012, **84**, 945.
- 45 A. Togo, F. Oba and I. Tanaka, *Phys. Rev. B: Condens. Matter Mater. Phys.*, 2008, **78**, 134106.
- 46 P. Giannozzi, S. Baroni, N. Bonini, M. Calandra, R. Car, C. Cavazzoni, D. Ceresoli, G. L. Chiarotti, M. Cococcioni and I. Dabo, *J. Phys.: Condens. Matter*, 2009, **21**, 395502.
- 47 W. McMillan, *Phys. Rev.*, 1968, **167**, 331.
- 48 M. Gajdoš, K. Hummer, G. Kresse, J. Furthmüller and F. Bechstedt, *Phys. Rev. B: Condens. Matter Mater. Phys.*, 2006, **73**, 045112.
- 49 M. Blanco, E. Francisco and V. Luana, *Comput. Phys. Commun.*, 2004, **158**, 57–72.
- 50 Y. Liang and B. Zhang, *Phys. Rev. B: Condens. Matter Mater. Phys.*, 2007, **76**, 132101.
- 51 F. Birch, *Phys. Rev.*, 1947, **71**, 809.
- 52 R. J. Angel, *Rev. Mineral. Geochem.*, 2000, **41**, 35–59.
- 53 R. Hill, *Proc. Phys. Soc. A*, 1952, **65**, 349.
- 54 M. Born and K. Huang, *Dynamical Theory of Crystal Lattices*, Oxford University, New York, 1998.
- 55 J. Muscat, V. Swamy and N. M. Harrison, *Phys. Rev. B: Condens. Matter Mater. Phys.*, 2002, **65**, 224112.
- 56 M. E. Kilic and K. R. Lee, *Phys. Rev. Mater.*, 2021, **5**, 065404.
- 57 M. E. Kilic and K. R. Lee, *Carbon*, 2021, **174**, 368–381.
- 58 M. E. Kilic and K. R. Lee, *Carbon*, 2022, **195**, 154–164.
- 59 J. Li, X. Dai, S. Liang, K. Tai, Y. Kong and B. Liu, *Phys. Rep.*, 2008, **455**, 1–134.

